

1 **Evolution of droplet size distributions during the**
2 **transition of an ultraclean stratocumulus cloud system**
3 **to open cell structure: an LES investigation using**
4 **Lagrangian microphysics**

5 **Kamal Kant Chandrakar ¹, Hugh Morrison ¹, and Mikael Witte ²**

6 ¹National Center for Atmospheric Research, Boulder, CO 80307

7 ²Naval Postgraduate School, Monterey, CA 93943

8 **Key Points:**

- 9 • The first Lagrangian microphysics simulation of the stratocumulus transition from
10 closed to open cell structure is documented
11 • During the transition, the rain rate increases sharply as the coalescence timescale
12 decreases relative to the large eddy turnover
13 • Drop size distributions in open cell stratocumulus are broader in downdrafts than
14 updrafts from coalescence, evaporation and drop mixing

Corresponding author: Kamal Kant Chandrakar, kkchandr@ucar.edu

This article has been accepted for publication and undergone full peer review but has not been through the copyediting, typesetting, pagination and proofreading process, which may lead to differences between this version and the [Version of Record](#). Please cite this article as [doi: 10.1029/2022GL100511](https://doi.org/10.1029/2022GL100511).

This article is protected by copyright. All rights reserved.

Abstract

A state-of-the-art Lagrangian microphysics scheme is used in a large-eddy simulation to investigate the stratocumulus transition from closed to open cell structure. Processes controlling precipitation development, which is a key to the transition, are analyzed by leveraging unique benefits of Lagrangian microphysics, particularly the ability to track computational drops in the flow. Sufficient time is needed for coalescence growth of cloud drops to drizzle within the updraft-downdraft cycle of large eddies. This favors broad drop size distributions (DSDs) and drizzle growth in downdrafts, where drops are typically much older than in updrafts. During the closed cell stage, mean cloud drop radius is too small, and the DSDs are too narrow, so that the timescale for coalescence is much longer than the large eddy turnover time and drizzle growth is limited. The closed-to-open cell transition occurs when these timescales become comparable and the precipitation flux increases sharply.

Plain Language Summary

Low-level stratocumulus clouds critically impact Earth's energy budget by reflecting incoming solar radiation. Accurate representation of these shallow clouds in climate models requires information on fine-scale cloud properties and processes (e.g., cloud and drizzle drop sizes and their growth) due to significant variability driven by turbulent flow. Sufficient drizzle formation in these clouds changes their flow structure, shifting clouds from a uniform layer to a layer with an open cell structure. Using a state-of-the-art particle-based cloud model, this study showed that cloud droplet sizes and their coalescence growth change during this process in a way that sharply enhances precipitation. Once the clouds change to an open structure, cloud and drizzle drop sizes and growth differ in upward and downward moving branches of large turbulent eddies, with more drizzle formation and variation in drop sizes in downward flow regions. Information on the drop size variability and growth presented here could lead to better representation of clouds in climate models and measurements using ground and satellite-based instruments.

1 Introduction

Shallow boundary layer clouds remain a large source of uncertainty in global climate models. Complex, multi-scale interactions between large-scale dynamics, turbulence, microphysics, and radiation are a critical challenge in parameterizing these clouds (Wood, 2012). Aerosol-cloud-precipitation interactions strongly affect micro- and macro-scale cloud properties and processes, which have been shown, for example, to drive a transition of stratocumulus from closed to open or open to closed cellular structure (Wood, 2012; Stevens et al., 2005; Savic-Jovicic & Stevens, 2008; Wood et al., 2008; H. Wang & Feingold, 2009; Goren & Rosenfeld, 2012). Closed and open cellular regions differ not just dynamically but also in cloud properties and radiative forcing. Thus, accurate representation of these transitions are important for the overall radiative forcing in Earth system models.

Previous modeling studies of closed-to-open cell transitions mainly used bulk microphysics schemes with highly idealized representations of aerosol processing (e.g., Savic-Jovicic & Stevens, 2008; H. Wang & Feingold, 2009; Kazil et al., 2011; Feingold et al., 2015, and others). Bulk microphysics schemes have limitations due to assumptions regarding the shape of droplet size distributions (DSDs) and simplified process rates formulations (Khain et al., 2015; Morrison et al., 2020). Simulations using DSD-resolving microphysics schemes (e.g., Magaritz et al., 2009; Andrejczuk et al., 2010; Witte et al., 2019; Hoffmann & Feingold, 2019, and others) used domains too small to capture the mesoscale dynamics of closed-to-open cell transitions. As a result, understanding of the processes driving DSD evolution during these transitions is limited. This is an impor-

64 tant knowledge gap because DSD properties critically impact precipitation development
65 (Pruppacher & Klett, 1997), radiative forcing (Martin et al., 1994; Liu & Daum, 2000),
66 and dynamical feedbacks (e.g., S. Wang et al., 2003; Ackerman et al., 2004; Bretherton
67 et al., 2007; Mellado, 2017). To address this gap, we performed the first (to our knowl-
68 edge) large-eddy-simulation (LES) of a closed-to-open cell transition using Lagrangian
69 cloud microphysics (the super-droplet method SDM, Shima et al., 2009) with explicit
70 aerosol activation, scavenging, and processing. SDM tracks Lagrangian trajectories of
71 “super-droplets” (computational particles) which represent a multitude of real drops hav-
72 ing identical properties in the flow. This approach has several advantages over traditional
73 Eulerian bin schemes, including eliminating numerical diffusion of cloud variables, ex-
74 plicit representation of aerosol processes by tracking cloud-borne aerosol in super-droplets,
75 and ability to represent stochastic aspects of drop collision-coalescence (Jaruga & Pawlowska,
76 2018; Morrison et al., 2018; Grabowski et al., 2019; Chandrakar et al., 2022).

77 Using this novel modeling framework, we address several outstanding questions relat-
78 ed to stratocumulus evolution: 1) How do DSDs vary spatially and temporally dur-
79 ing the closed-to-open cell transition? 2) What are the processes associated with this vari-
80 ability? 3) How do these processes contribute to the increased precipitation flux driv-
81 ing the cellular transition? Supersaturation variability is hypothesized to cause DSD broad-
82 ening in a clean environment (e.g., Chandrakar et al., 2016; Glienke et al., 2017). In ad-
83 dition to the influence of changing aerosol size and concentration through cloud process-
84 ing and scavenging, the impact of supersaturation variability on DSD width may vary
85 during the transition (Chandrakar et al., 2017). We address these questions using model
86 data and qualitatively compare simulated DSD outputs with observations of drizzling
87 stratocumulus during the CSET (Cloud System Evolution in the Trades) field campaign
88 (Albrecht et al., 2019). While the main goal of this work is to improve understanding
89 of microphysical processes during the transition, it is also relevant to bulk cloud param-
90 eterizations.

91 2 Overview of The Simulation Setup

92 We simulate the closed-to-open cell transition with a standard case of drizzling ma-
93 rine stratocumulus (the second research flight (RF02) of the Dynamics and Chemistry
94 of Marine Stratocumulus (DYCOMS-II) (Ackerman et al., 2009) using Lagrangian mi-
95 crophysics (SDM) in a LES framework (Cloud Model 1, CM1, Bryan & Fritsch, 2002).
96 Lagrangian microphysics is uniquely suited for the closed-to-open cell stratocumulus prob-
97 lem because of its detailed treatment of aerosol processing and ability to track compu-
98 tational drops in the flow. The CM1-SDM setup and its advantages compared to Eu-
99 lerian bin schemes are discussed in detail in the Supplemental Information (SI). We fol-
100 low the default case specifications except initial winds and large-scale shear are set to
101 zero and the initial aerosol concentration is reduced by a factor of five to accelerate the
102 transition. The computational domain is $50 \times 25 \text{ km}^2$ horizontally and 1.5 km verti-
103 cally, and the horizontal and vertical grid spacings are 100 m and 5 m, respectively.

104 3 Results and Discussion

105 3.1 Transition of the cloud field from closed to open cellular structure

106 Figure 1a-b shows differences in the modeled cloud field during the closed (earlier)
107 and open cell (later) phases. Well-documented (e.g., Wood, 2012) features of stratocu-
108 mulus convection are evident: more extensive cloud cover with smaller and weaker up-
109 drafts and little precipitation during the closed cell phase versus less cloud cover but stronger,
110 more concentrated updrafts and substantial precipitation during the open cell phase. Fig-
111 ure 2 displays the evolution of different cloud quantities during the cellular transition.
112 After an initial spin-up period, mean in-cloud cloud water mixing ratio (q_{c_m}) increases
113 slowly to a peak at ~ 4 hr (Fig. 2a); hereafter “in-cloud” refers to grid cells with $qc \geq$

114 10^{-5} kg kg⁻¹ and 40 μ m drop radius R separates cloud and rain. During this period,
 115 mean in-cloud rainwater mass (qr_m) and number mixing ratios also increase, but at a
 116 marginal rate. The liquid and cloud water paths (LWP and CWP) also peak between
 117 3-4 hr (Fig. 2b). After an initial decrease, cloud droplet number concentration (n_d) is
 118 nearly constant between 2-3.5 hr (Fig. 2c), indicating a balance between loss from co-
 119 alescence and evaporation and generation by droplet activation, and thereafter it decreases.

120 A key aspect of microphysical evolution is the DSD width, quantified here by the
 121 radius standard deviation σ_R in a grid cell. The mean σ_R (averaged over all in-cloud grids)
 122 closely follows the time evolution of supersaturation standard deviation σ_s , consistent
 123 with DSD broadening from mixing of drops experiencing different supersaturations and
 124 growth histories. Both σ_R and σ_s peak around 2 hr coinciding with the peak entrainment
 125 velocity, decrease between 2 and 3.5 hr, and increase steadily thereafter. These trends
 126 closely follow those of the phase relaxation timescale $\tau_c \equiv (4\pi\alpha n_d R)^{-1}$ (Fig. 2f), the
 127 response timescale of the droplet population to a change in the supersaturation field. Here,
 128 α is a thermodynamic factor (Politovich & Cooper, 1988).

129 Precipitation-generated asymmetry in the vertical cooling profile is a critical driver
 130 of the cellular transition (Feingold et al., 2010). What processes in turn control precip-
 131 itation rate? Drops must spend sufficient time inside cloud to grow to drizzle size by collision-
 132 coalescence. This implies that the characteristic timescale for coalescence $\tau_{col} \equiv (qc_m +$
 133 $qr_m)/A_c$ must be similar to or less than the eddy turnover timescale (Feingold et al., 1996)
 134 $\tau_{tw} \equiv H/\sigma_w$ for significant precipitation generation. Here, H is the average cloud layer
 135 depth, σ_w^2 is the in-cloud resolved w variance, and A_c is the integral mass transfer rate
 136 towards larger sizes from the coalescence of drop pairs in a grid cell. Figure 2f shows how
 137 these timescales change during the transition. The coalescence timescale increases from
 138 about 1500 to 1800 sec between 2 and 3 hours owing to the decrease of σ_R (narrower DSDs).
 139 However, after this time it decreases quickly – meaning faster coalescence – as both mean
 140 radius and σ_R increase. In contrast, the eddy turnover time is relatively steady with only
 141 a small increase from about 700 to 900 sec between 3 and 7 hr. τ_{col} approaches τ_{tw} be-
 142 tween ~ 4.5 and 5.5 hr, and the surface precipitation rate P correspondingly increases
 143 rapidly (Fig. 2c). At 5.7 hr, τ_{col} crosses over and becomes smaller than τ_{tw} , and P con-
 144 tinues to increase until ~ 6.5 hr.

145 Scavenging of aerosols is an underlying driver of microphysical changes during the
 146 transition. Figure 3f,i shows evolution of the aerosol size distribution (concentration dis-
 147 tributions and normalized PDFs, including interstitial and cloud-borne aerosol). Aerosol
 148 number loss occurs over time due to scavenging and drop coalescence, driving a reduc-
 149 tion of n_d and increase in mean drop radius after 3.5 hr (Fig. 3c-d). Smaller aerosols in
 150 the simulation have lower probability of activation and subsequent removal through drop
 151 coalescence. Thus, their loss is slower over time. While there is a decrease in the con-
 152 centration of all aerosol sizes less than ~ 600 nm, the largest relative decrease is for sizes
 153 between 20 and 200 nm (Fig. 3f). Over time, the normalized PDFs exhibit a shift in the
 154 relative concentrations from 20-200 nm to sizes greater than 300 nm (Fig. 3i). Coales-
 155 cence produces large drops, many of which evaporate and regenerate giant cloud con-
 156 densation nuclei (CCN). These large CCN can easily grow to form relatively large drops
 157 (Jensen & Nugent, 2017), contributing to DSD broadening in updrafts near cloud base.
 158 However, such an impact is small overall and other processes (e.g., supersaturation vari-
 159 ability) dominate DSD broadening in the ultraclean condition in this simulation. For higher
 160 background CCN concentrations, the impact of large CCN could be more significant ini-
 161 tially, but supersaturation being more important once the cloud system becomes clear.

162 3.2 Evolution of DSDs during the closed-to-open cell transition

163 We next show DSD evolution at different altitudes during the stratocumulus transi-
 164 tion to open cellular convection (Fig. 3). The DSDs in this figure are normalized (giv-

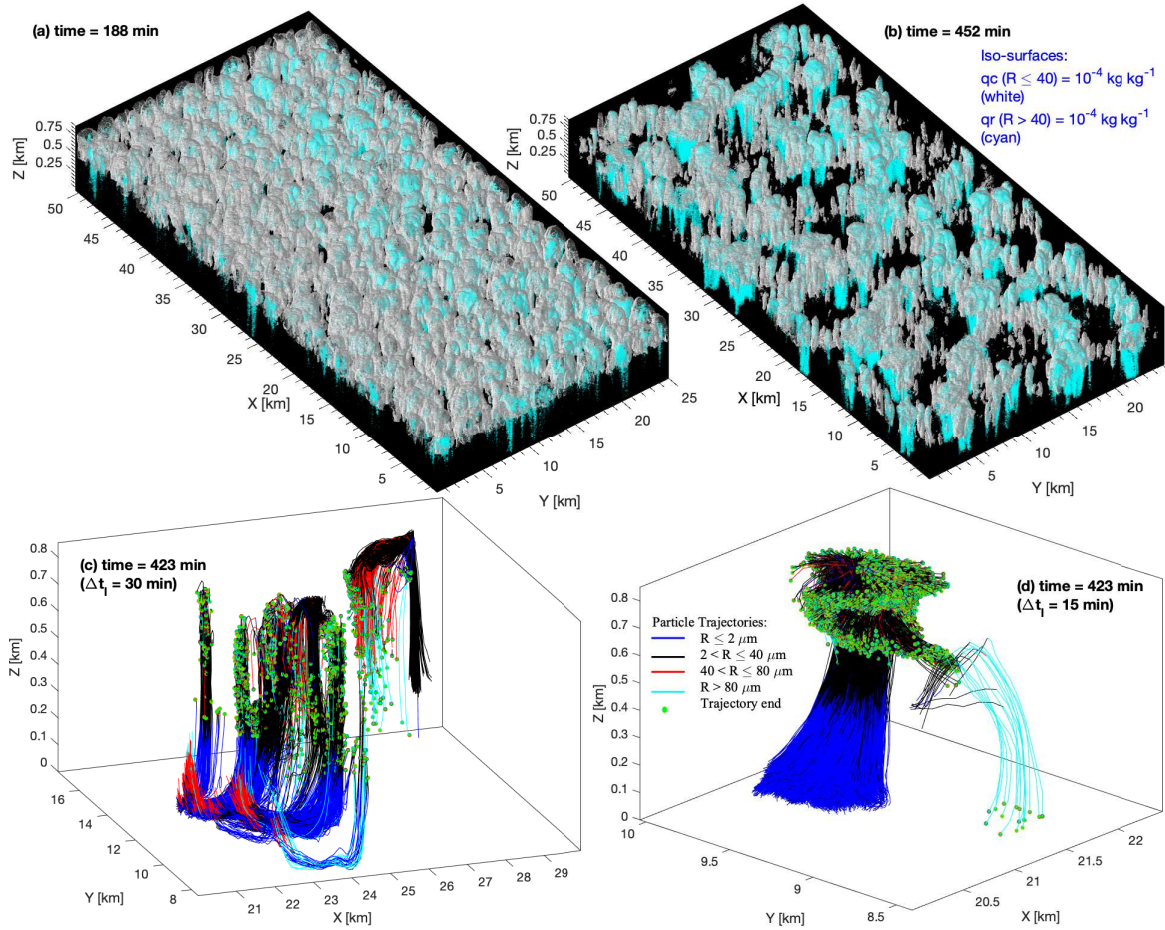


Figure 1. (a)-(b) Iso-surfaces of cloud (qc) and rain water (qr) mixing ratio during the closed- and open-cell phases. (c)-(d) Sample super-droplet trajectories for time periods (Δt_i) of 30 min (c) and 15 min (d) during the open-cell phase. Trajectories in (c) were selected based on a minimum length of 1000 m and in (d) by a minimum length of 800 m and end radius $R > 10 \mu\text{m}$, respectively.

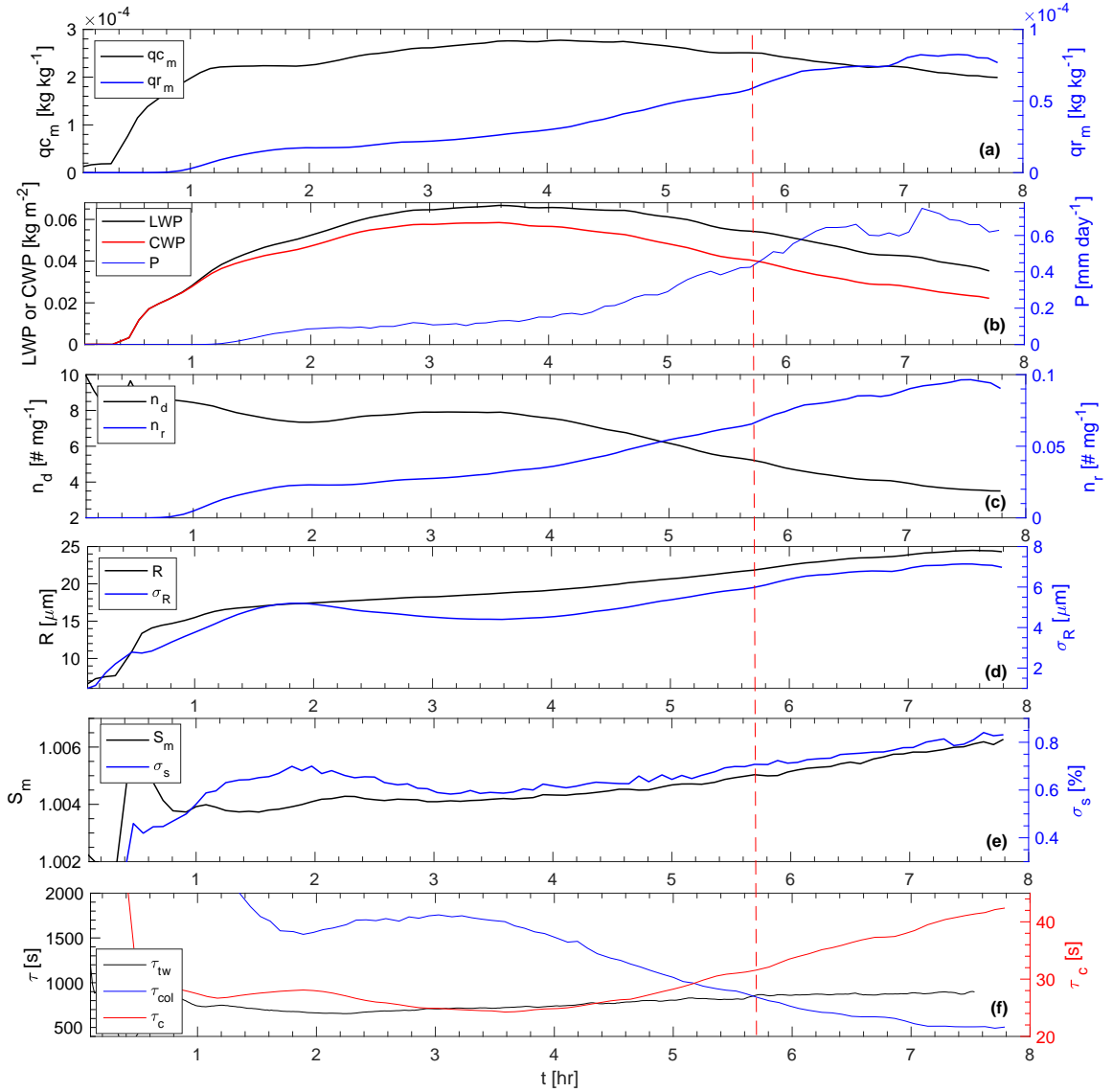


Figure 2. Timeseries of mean (a) cloud water (q_{c_m}) and rainwater (q_{r_m}) mixing ratios; (b) cloud droplet number (n_d) and raindrop number (n_r) mixing ratios; (c) domain-mean cloud water path (CWP), liquid water path (LWP, cloud plus rain) paths, and surface precipitation rate (P); (d) mean (R) and standard deviation (σ_R) of droplet radius; (e) mean (S_m) and standard deviation (σ_s) of supersaturation for grids with vertical velocity $w \geq 0 \text{ m s}^{-1}$; and (f) mean in-cloud eddy turnover (τ_{tw}), collision-coalescence (τ_{col}), and phase relaxation timescales (τ_c). The vertical dashed line indicates the closed-to-open cell transition time (defined here by cloud cover $< 60\%$). Quantities in (a), (b), (d), (e), and (f) are calculated for in-cloud points. Note σ_s is calculated from the resolved supersaturation field.

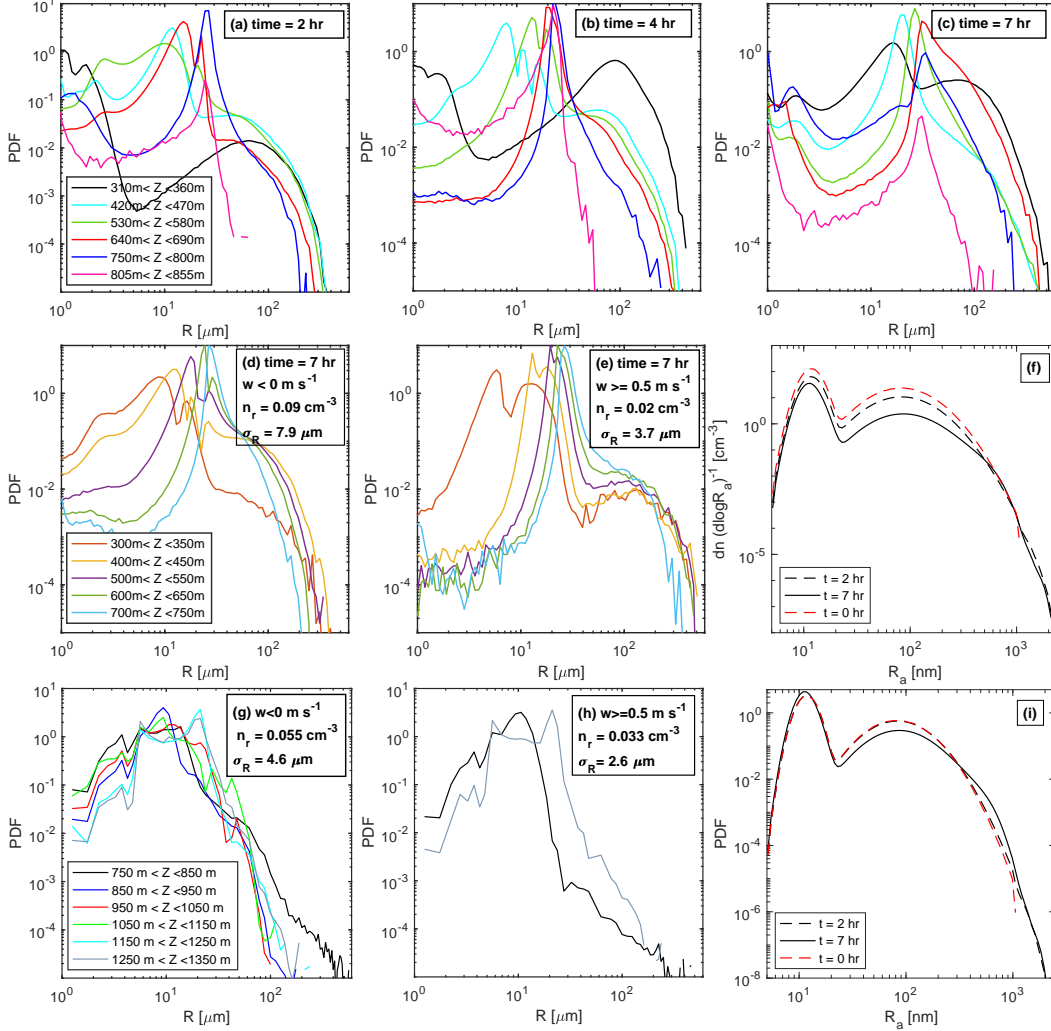


Figure 3. (a)-(c) DSDs averaged over grid cells with $qc + qr \geq 10^{-5} \text{ kg kg}^{-1}$ at different altitude (Z) ranges and at different times during closed-to-open cell transition. (d)-(e) DSDs averaged over in-cloud grid cells at different w and Z ranges during the open cellular phase. (g)-(h) Average merged DSDs measured in open cell stratocumulus during CSET flight RF14 (see SI for details). (f),(i) Total aerosol (interstitial plus cloud-borne) dry solute radius (R_a) distributions averaged over $200 \leq Z \leq 700 \text{ m}$ initially and during the closed and open cell phases. (f) shows the aerosol distribution in terms of concentration, and (i) the normalized PDF.

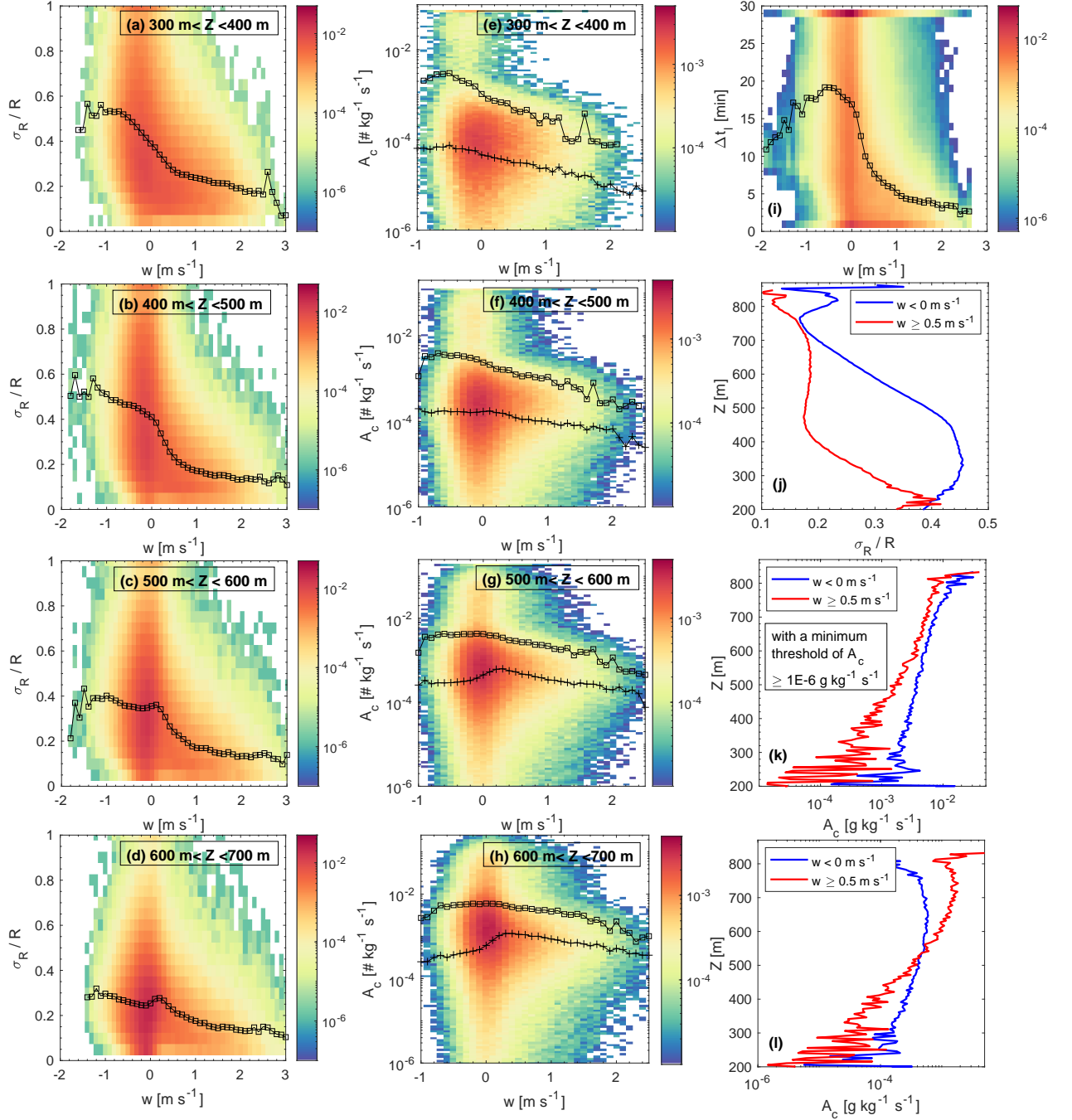


Figure 4. Variation of (a)-(d) relative dispersion (σ_R/R), (e)-(h) coalescence rate (A_c), and (i) drop lifetime (Δt_ℓ) with vertical velocity w . σ_R/R and A_c include data from all cloudy grid cells. (j)-(l) In-cloud average vertical profiles of σ_R/R and A_c in downdrafts ($w < 0 \text{ m s}^{-1}$) and strong updrafts ($w \geq 0.5 \text{ m s}^{-1}$). All results in this figure are from the open cell phase. Note, individual particle data is sampled for 30 min during the open cell phase, and thus the lifetime of some drops could be longer than that. The coalescence rate is the integral mass transfer rate from smaller to larger drops from the coalescence of drop pairs in a grid cell. The colorbars show normalized counts for each w bin. Mean A_c values in (e)-(h) calculated using a threshold of $10^{-6} \text{ g kg}^{-1} \text{ s}^{-1}$ are denoted by squares while pluses show mean values without the threshold.

ing $\int PDF(R)d(\log R) = 1$), to focus on variations in DSD shape and width rather than total concentration. As expected, the average DSDs in grid cells with $qc+qr \geq 10^{-5} \text{ kg kg}^{-1}$ (Fig. 3a-c) have an increasing cloud mode radius with height owing to condensational growth. During the initial phase of the transition at 2 hr, significant droplet activation and variability in the activation height generate broad DSDs, especially toward small sizes, consistent with the hypothesis of variable lifting condensation level (Considine & Curry, 1996). Mixing of drops experiencing different supersaturation and growth histories also leads to fairly broad DSDs above cloud base. This compensates for narrowing of DSDs from condensational growth caused by the inverse radius dependence of the drop growth rate. A similar picture holds at 4 hr during the closed-to-open cell transition, although there is greater DSD narrowing with height than at 2 hr consistent with reduced supersaturation variability at this time (see Fig. 2e). DSDs at the top are broader towards smaller sizes due to entrainment-induced activation.

At 7 hr, after transitioning to the open cell regime, the left (small) tail of the DSDs is suppressed because of reduced in-cloud droplet activation, but there is significant broadening of mean DSDs toward the right (large) tail. Broadening in pristine conditions is consistent with the hypothesis of broadening from variable supersaturation history presented in Chandrakar et al. (2016) and Chandrakar et al. (2017) based on laboratory experiments as well as field observations in Glienke et al. (2017). Significant collision-coalescence during the open cell phase at 7 hr also contributes to DSD broadening, leading to a wide shoulder from the cloud mode toward drizzle sizes ($R > 40 \mu\text{m}$). Even though a weak drizzle mode is evident at 2 and 4 hr, mainly near cloud base, the concentration of drops in the cloud mode decreases sharply at $R > 40 \mu\text{m}$.

3.3 Dependence of droplet size distributions on vertical velocity

Interactions between the microphysics and cloud dynamics are highlighted by sample particle trajectories during the open cell period in Fig. 1c-d. The 30 min trajectories in (c) trace boundary layer large eddies. Some trajectories show evaporation of drizzle drops (red) in downdrafts below cloud base to regenerate CCN (blue), ingestion of these CCN into updrafts, their subsequent activation as cloud droplets (black), and ultimately drizzle formation (red and cyan). Other trajectories show re-circulation of drizzle drops from downdrafts to updrafts without complete evaporation. Near cloud top, some cloud droplets grow to drizzle sizes through collision-coalescence, whereas others evaporate in downdrafts. The shorter 15 min trajectories with a zoomed-in view in (d) clearly demonstrate cloud droplet activation (blue to black), growth (black to red), and lateral transport at different altitudes near cloud top. Interestingly, some trajectories in both (c) and (d) show rapid growth of cloud droplets to drizzle from collision-coalescence, mainly within downdrafts; the vast majority of drops with radius $> 80 \mu\text{m}$ occur in downdrafts, with some reaching the surface. Overall, these trajectories clearly show variability in growth history at each altitude and mixing of particles in different cloud regions.

To investigate the spatial variability of DSDs and their dependence on cloud dynamics during the open cell phase further, we classified DSDs based on vertical velocity w (Figure 3d-e). DSDs are narrower for both the left and right tails in relatively strong updrafts ($w > 0.5 \text{ m s}^{-1}$, which we will refer to as “strong” updrafts) compared to downdrafts ($w < 0 \text{ m s}^{-1}$). In strong updrafts, there is a narrowing of the DSDs with altitude above cloud base from condensation due to large mean supersaturation and limited mixing of drops with different growth histories (Fig. 3e). In contrast, evaporation in downdrafts causes broadening to small drop sizes at lower and middle cloud levels (Fig. 3d). The interface between strong updraft and downdraft regions also has fairly broad DSDs due to mixing of drops with different growth histories (see Figure S5). Mixing also contributes to DSD broadening within both updraft and downdraft regions, although it is compensated by DSD narrowing from condensation in updrafts.

216 A key difference between updraft and downdraft DSDs is the wide shoulder of drizzle
 217 drops extending to the right of the main cloud mode in the downdraft DSDs, which
 218 is mostly absent in strong updrafts (Fig. 3d-e). Correspondingly, the mean concentra-
 219 tion of drizzle drops with radius $> 40 \mu\text{m}$ is 4.5 times larger in downdrafts than strong
 220 updrafts (0.09 versus 0.02 cm^{-3}). The mean concentration of drizzle drops in downdrafts
 221 also increases with decreasing altitude within the cloud. This is caused by additional co-
 222 alescence growth in downdrafts consistent with our trajectory analysis. Figure 4e-h, k-
 223 l, which shows frequency distributions of coalescence rate (integral mass transfer rate from
 224 small to large drops associated with all collision pairs) as a function of vertical velocity
 225 and mean coalescence rate profiles in updrafts and downdrafts, confirms strong coales-
 226 cence growth in downdrafts ($w < 0$) at all cloud levels. Near cloud base, mean coales-
 227 cence rates within the cloud are about an order of magnitude greater in downdrafts com-
 228 pared to updrafts (Fig. 4e, k, l). Without applying any threshold, mean coalescence rates
 229 are lower in downdrafts than strong updrafts above 550 m. However, large coalescence
 230 rates ($\geq 10^{-2} \text{ g kg}^{-1} \text{ s}^{-1}$) occur predominately in downdrafts at all altitudes within the
 231 cloud. This behavior is consistent with substantial inhomogeneity and skewness of the
 232 coalescence rate distribution in downdrafts. Transport of smaller drops from updraft and
 233 significant evaporation from entrainment, suppressing drop coalescence in some down-
 234 draft grid cells, could be partly responsible for this strong inhomogeneity.

235 Why are downdraft regions favored for large coalescence growth rates? An anal-
 236 ysis of cloud/drizzle drop lifetimes sheds light on this question (Fig. 4i). The drop life-
 237 time is defined as the period over which $R > 1 \mu\text{m}$ during the previous 30 min sam-
 238 pling. There is large variability in drop lifetime at all vertical velocities, while the mean
 239 lifetime is generally > 15 min in downdrafts, similar to (or greater than) the eddy turnover
 240 time, but < 5 min in strong updrafts. These results are consistent with (Kogan, 2006),
 241 who analyzed in-cloud residence time of air parcels in LES of stratocumulus rather than
 242 drop trajectories. Our results therefore give the following conceptual picture of micro-
 243 physical evolution in open cell stratocumulus convection: generation of new cloud droplets
 244 by activation near cloud base, their ascent and condensational growth in updrafts, trans-
 245 port to downdrafts, and accelerated coalescence growth in downdrafts as the drops con-
 246 tinue to age. In other words, large drops are favored in downdrafts because it takes time
 247 for coalescence growth to occur over the course of one large eddy turnover. Before the
 248 transition to open cells, the coalescence timescale is much longer than one eddy turnover
 249 time, and hence there is not enough time for significant coalescence growth in an updraft-
 250 downdraft cycle. In this case, the mean DSDs resemble the relatively narrow DSDs in
 251 updrafts in the open cell regime, particularly at the cloud DSD mode and to its right.
 252 Once the coalescence timescale becomes similar to the eddy turnover timescale, coales-
 253 cence growth is enhanced and there is a rapid shift from non-precipitating (or barely-
 254 precipitating) to precipitating regimes.

255 Differences in modeled DSDs between updrafts and downdrafts are generally con-
 256 sistent with observations of drizzling stratocumulus (open cellular) during CSET (Fig.
 257 3g-h). The mode radius of the observed mean DSDs increases, and the left tail decreases
 258 with altitude as expected. Both the right and left tails near the primary mode are broader
 259 in downdrafts than in updrafts. There is a broad shoulder extending from the DSD mode
 260 toward drizzle drop sizes in downdrafts but a sharp drop in concentration to the right
 261 of the mode in strong updrafts. Correspondingly, the mean σ_R is about a factor of two
 262 larger in downdrafts than in updrafts from both the model and observations, although
 263 the modeled σ_R values are larger by $\sim 1-3 \mu\text{m}$. Similarly, the observed mean drizzle
 264 drop concentration (radius $> 40 \mu\text{m}$) is a factor of 1.7 higher in downdrafts than in strong
 265 updrafts, qualitatively similar to the updraft/downdraft differences in the simulation though
 266 somewhat smaller in magnitude. These findings are also consistent with measurements
 267 for another case with a lower droplet concentration (see Figure S4).

Investigating the relationship between DSD width and cloud dynamics (vertical velocity) is relevant to bulk microphysics schemes, many of which make assumptions about the DSD width typically quantified by the relative dispersion, σ_R/R . Figure 4a-d,j shows the variation of σ_R/R with vertical velocity and altitude. For a given altitude range, mean σ_R/R is fairly constant with vertical velocity for downdrafts but with a sharp decrease at vertical velocities between roughly -0.5 and 0.5 m s^{-1} . It then decreases slightly with increasing vertical velocity for $w > 0.5$ m s^{-1} . This trend of σ_R/R is consistent with the DSDs in Fig. 3 indicating much broader DSDs in downdrafts than updrafts, toward both small and large drop sizes. Note that trends in σ_R are similar to σ_R/R . This spatial structure of DSD width is neglected in bulk microphysics schemes, likely impacting modeled cloud-radiative interactions since cloud droplet effective radius depends on σ_R/R (Martin et al., 1994). Furthermore, with a few exceptions (e.g., Seifert & Beheng, 2001; Liu & Daum, 2004), most autoconversion formulations in bulk schemes (representing the conversion of cloud droplets to drizzle/rain via coalescence) do not include a dependence on DSD width. Such schemes may therefore struggle to represent correctly the preferential growth of drizzle drops in downdrafts related to the coalescence timescale and large eddy turnover. This in turn could impact simulation of other features tied to precipitation using bulk schemes, including aerosol scavenging and the closed-to-open cell dynamical transition itself.

4 Conclusions

We investigated DSD evolution and variability in an ultraclean environment during a stratocumulus closed-to-open cell transition using LES coupled with a particle-based Lagrangian cloud microphysics scheme. This scheme is uniquely suited for the problem since it gives the Lagrangian growth and transport history of individual computational particles, explicitly tracks cloud-borne aerosol, and has other numerical advantages outlined in the introduction. As suggested in past studies (see Wood, 2012, and references therein), the development of precipitation is a key driver of the closed-to-open cell transition. We showed that a decrease in the collision-coalescence timescale relative to the large eddy-turnover timescale triggers a sharp increase in surface precipitation. The collision-coalescence timescale depends on other microphysical process timescales relative to the dynamics that control the DSD shape, for example, aerosol scavenging and phase relaxation timescales. Supersaturation variability and mixing of droplets with different growth histories also contribute to the transition through their influence on DSD width. Sufficient drop residence time within a large eddy updraft-downdraft cycle is needed for growth to drizzle size via coalescence, favoring coalescence growth of older drops in downdrafts. In contrast, DSDs in updrafts are narrower and comprise mainly younger drops. Prior to the open cell transition, the timescale for coalescence growth is long relative to the eddy turnover time, DSDs are narrow and precipitation is hampered. These results highlight how spatial and temporal variability of DSDs is a key feature of the closed-to-open cell transition. This variability cannot be represented in current bulk microphysics schemes that assume constant cloud DSD dispersion or relate it to droplet number concentration (e.g., Thompson et al., 2008; Morrison et al., 2009), which potentially explains why the bifractal structure of rain produced by these schemes in LES is minimally intermittent and overly smooth compared to observations (Witte et al., 2022). Relationships between DSD dispersion, collision-coalescence rate, and vertical velocity identified in this study could help improve bulk schemes as well as remote sensing retrievals.

Open Research

CM1 code with detail documentation is available at <https://www2.mmm.ucar.edu/people/bryan/cm1/>. SDM code provided by Shin-ichiro Shima is available at <https://doi.org/10.5281/zenodo.3483650>. The CSET field data used in this study is avail-

318 able at (<https://doi.org/10.5065/D65Q4T96>) (UCAR/NCAR-Earth Observing Lab-
319 oratory, 2018).

320 Acknowledgments

321 This material is based upon work supported by the National Center for Atmospheric Re-
322 search, which is a major facility sponsored by the National Science Foundation under
323 Cooperative Agreement No. 1852977. This work was also supported by U.S. Department
324 of Energy Atmospheric System Research grant DE-SC0020118 (HM) and DE-SC0020332
325 (MKW). KKC was supported by the NCAR ASP postdoctoral fellowship program. We
326 acknowledge high-performance computing support from Cheyenne (doi:10.5065/D6RX99HX)
327 provided by NCAR's Computational and Information Systems Laboratory, sponsored
328 by the National Science Foundation.

329 References

- 330 Ackerman, A. S., Kirkpatrick, M. P., Stevens, D. E., & Toon, O. B. (2004). The
331 impact of humidity above stratiform clouds on indirect aerosol climate forcing.
332 *Nature*, *432*(7020), 1014–1017.
- 333 Ackerman, A. S., VanZanten, M. C., Stevens, B., Savic-Jovicic, V., Bretherton,
334 C. S., Chlond, A., ... others (2009). Large-eddy simulations of a drizzling,
335 stratocumulus-topped marine boundary layer. *Monthly Weather Review*,
336 *137*(3), 1083–1110.
- 337 Albrecht, B., Ghate, V., Mohrmann, J., Wood, R., Zuidema, P., Bretherton, C., ...
338 others (2019). Cloud system evolution in the trades (cset): Following the
339 evolution of boundary layer cloud systems with the nsf–ncar gv. *Bulletin of the*
340 *American Meteorological Society*, *100*(1), 93–121.
- 341 Andrejczuk, M., Grabowski, W., Reisner, J., & Gadian, A. (2010). Cloud-aerosol
342 interactions for boundary layer stratocumulus in the lagrangian cloud model.
343 *Journal of Geophysical Research: Atmospheres*, *115*(D22).
- 344 Bretherton, C., Blossey, P. N., & Uchida, J. (2007). Cloud droplet sedimentation,
345 entrainment efficiency, and subtropical stratocumulus albedo. *Geophysical re-*
346 *search letters*, *34*(3).
- 347 Bryan, G. H., & Fritsch, J. M. (2002). A benchmark simulation for moist nonhydro-
348 static numerical models. *Monthly Weather Review*, *130*(12), 2917–2928.
- 349 Chandrakar, K. K., Cantrell, W., Chang, K., Ciochetto, D., Niedermeier, D.,
350 Ovchinnikov, M., ... Yang, F. (2016). Aerosol indirect effect from turbulence-
351 induced broadening of cloud-droplet size distributions. *Proceedings of the*
352 *National Academy of Sciences*, *113*(50), 14243–14248.
- 353 Chandrakar, K. K., Cantrell, W., Ciochetto, D., Karki, S., Kinney, G., & Shaw, R.
354 (2017). Aerosol removal and cloud collapse accelerated by supersaturation
355 fluctuations in turbulence. *Geophysical Research Letters*, *44*(9), 4359–4367.
- 356 Chandrakar, K. K., Morrison, H., Grabowski, W. W., & Bryan, G. H. (2022). Com-
357 parison of lagrangian super-droplet and eulerian double-moment spectral mi-
358 crophysics schemes in large-eddy simulations of an isolated cumulus-congestus
359 cloud. *Journal of the Atmospheric Sciences*.
- 360 Considine, G., & Curry, J. A. (1996). A statistical model of drop-size spectra for
361 stratocumulus clouds. *Quarterly Journal of the Royal Meteorological Society*,
362 *122*(531), 611–634.
- 363 Feingold, G., Koren, I., Wang, H., Xue, H., Brewer, W., et al. (2010). Precipitation-
364 generated oscillations in open cellular cloud fields. *Nature*, *466*(7308), 849–
365 852.
- 366 Feingold, G., Koren, I., Yamaguchi, T., & Kazil, J. (2015). On the reversibility of
367 transitions between closed and open cellular convection. *Atmospheric Chem-*
368 *istry and Physics*, *15*(13), 7351–7367.

- 369 Feingold, G., Stevens, B., Cotton, W., & Frisch, A. (1996). The relationship between
 370 drop in-cloud residence time and drizzle production in numerically simulated
 371 stratocumulus clouds. *Journal of the atmospheric sciences*, *53*, 1108–1122.
- 372 Glienke, S., Kostinski, A., Fugal, J., Shaw, R., Borrmann, S., & Stith, J. (2017).
 373 Cloud droplets to drizzle: Contribution of transition drops to microphysical
 374 and optical properties of marine stratocumulus clouds. *Geophysical Research
 375 Letters*, *44*(15), 8002–8010.
- 376 Goren, T., & Rosenfeld, D. (2012). Satellite observations of ship emission induced
 377 transitions from broken to closed cell marine stratocumulus over large areas.
 378 *Journal of Geophysical Research: Atmospheres*, *117*(D17).
- 379 Grabowski, W. W., Morrison, H., Shima, S.-I., Abade, G. C., Dziekan, P., &
 380 Pawlowska, H. (2019). Modeling of cloud microphysics: Can we do better?
 381 *Bulletin of the American Meteorological Society*, *100*(4), 655–672.
- 382 Hoffmann, F., & Feingold, G. (2019). Entrainment and mixing in stratocumulus:
 383 Effects of a new explicit subgrid-scale scheme for large-eddy simulations with
 384 particle-based microphysics. *Journal of the Atmospheric Sciences*, *76*(7),
 385 1955–1973.
- 386 Jaruga, A., & Pawlowska, H. (2018). libcloudph++ 2.0: aqueous-phase chemistry
 387 extension of the particle-based cloud microphysics scheme. *Geoscientific Model
 388 Development*, *11*(9), 3623–3645.
- 389 Jensen, J. B., & Nugent, A. D. (2017). Condensational growth of drops formed
 390 on giant sea-salt aerosol particles. *Journal of the atmospheric sciences*, *74*(3),
 391 679–697.
- 392 Kazil, J., Wang, H., Feingold, G., Clarke, A., Snider, J. R., & Bandy, A. (2011).
 393 Modeling chemical and aerosol processes in the transition from closed to open
 394 cells during vocals-rex. *Atmospheric Chemistry and Physics*, *11*(15), 7491–
 395 7514.
- 396 Khain, A., Beheng, K., Heymsfield, A., Korolev, A., Krichak, S., Levin, Z., ... oth-
 397 ers (2015). Representation of microphysical processes in cloud-resolving
 398 models: Spectral (bin) microphysics versus bulk parameterization. *Reviews of
 399 Geophysics*, *53*(2), 247–322.
- 400 Kogan, Y. L. (2006). Large-eddy simulation of air parcels in stratocumulus clouds:
 401 Time scales and spatial variability. *Journal of the atmospheric sciences*, *63*(3),
 402 952–967.
- 403 Liu, Y., & Daum, P. H. (2000). Spectral dispersion of cloud droplet size distri-
 404 butions and the parameterization of cloud droplet effective radius. *Geophysical
 405 research letters*, *27*(13), 1903–1906.
- 406 Liu, Y., & Daum, P. H. (2004). Parameterization of the autoconversion process. part
 407 i: Analytical formulation of the kessler-type parameterizations. *Journal of the
 408 atmospheric sciences*, *61*(13), 1539–1548.
- 409 Magaritz, L., Pinsky, M., Krasnov, O., & Khain, A. (2009). Investigation of droplet
 410 size distributions and drizzle formation using a new trajectory ensemble model.
 411 part ii: Lucky parcels. *Journal of the atmospheric sciences*, *66*(4), 781–805.
- 412 Martin, G., Johnson, D., & Spice, A. (1994). The measurement and parameteri-
 413 zation of effective radius of droplets in warm stratocumulus clouds. *Journal of
 414 Atmospheric Sciences*, *51*(13), 1823–1842.
- 415 Mellado, J. P. (2017). Cloud-top entrainment in stratocumulus clouds. *Annual Re-
 416 view of Fluid Mechanics*, *49*, 145–169.
- 417 Morrison, H., Thompson, G., & Tatarskii, V. (2009). Impact of cloud microphysics
 418 on the development of trailing stratiform precipitation in a simulated squall
 419 line: Comparison of one-and two-moment schemes. *Monthly weather review*,
 420 *137*(3), 991–1007.
- 421 Morrison, H., van Lier-Walqui, M., Fridlind, A. M., Grabowski, W. W., Harrington,
 422 J. Y., Hoose, C., ... others (2020). Confronting the challenge of modeling
 423 cloud and precipitation microphysics. *Journal of advances in modeling earth*

- 424 *systems*, 12(8), e2019MS001689.
- 425 Morrison, H., Witte, M., Bryan, G. H., Harrington, J. Y., & Lebo, Z. J. (2018).
 426 Broadening of modeled cloud droplet spectra using bin microphysics in an
 427 eulerian spatial domain. *Journal of the Atmospheric Sciences*, 75(11), 4005–
 428 4030.
- 429 Politovich, M. K., & Cooper, W. A. (1988). Variability of the supersaturation in cu-
 430 mulus clouds. *Journal of the atmospheric sciences*, 45(11), 1651–1664.
- 431 Pruppacher, H., & Klett, J. (1997). Microphysics of clouds and precipitation,
 432 springer publications.
- 433 Savic-Jovcic, V., & Stevens, B. (2008). The structure and mesoscale organization
 434 of precipitating stratocumulus. *Journal of the Atmospheric Sciences*, 65(5),
 435 1587–1605.
- 436 Seifert, A., & Beheng, K. D. (2001). A double-moment parameterization for sim-
 437 ulating autoconversion, accretion and selfcollection. *Atmospheric research*, 59,
 438 265–281.
- 439 Shima, S.-i., Kusano, K., Kawano, A., Sugiyama, T., & Kawahara, S. (2009). The
 440 super-droplet method for the numerical simulation of clouds and precipita-
 441 tion: A particle-based and probabilistic microphysics model coupled with a
 442 non-hydrostatic model. *Quarterly Journal of the Royal Meteorological Soci-
 443 ety: A journal of the atmospheric sciences, applied meteorology and physical
 444 oceanography*, 135(642), 1307–1320.
- 445 Stevens, B., Vali, G., Comstock, K., Wood, R., Van Zanten, M. C., Austin, P. H., ...
 446 Lenschow, D. H. (2005). Pockets of open cells and drizzle in marine stratocu-
 447 mulus. *Bulletin of the American Meteorological Society*, 86(1), 51–58.
- 448 Thompson, G., Field, P. R., Rasmussen, R. M., & Hall, W. D. (2008). Explicit fore-
 449 casts of winter precipitation using an improved bulk microphysics scheme. part
 450 ii: Implementation of a new snow parameterization. *Monthly Weather Review*,
 451 136(12), 5095–5115.
- 452 UCAR/NCAR-Earth Observing Laboratory. (2018). *CSET: Low Rate (LRT - 1 sps)
 453 Navigation, State Parameter, and Microphysics Flight-Level Data. Version 1.3.*
 454 (UCAR/NCAR - Earth Observing Laboratory. [https://doi.org/10.5065/
 455 D65Q4T96](https://doi.org/10.5065/D65Q4T96). Accessed 06 May 2022.)
- 456 Wang, H., & Feingold, G. (2009). Modeling mesoscale cellular structures and drizzle
 457 in marine stratocumulus. part i: Impact of drizzle on the formation and evolu-
 458 tion of open cells. *Journal of the Atmospheric Sciences*, 66(11), 3237–3256.
- 459 Wang, S., Wang, Q., & Feingold, G. (2003). Turbulence, condensation, and liq-
 460 uid water transport in numerically simulated nonprecipitating stratocumulus
 461 clouds. *Journal of the atmospheric sciences*, 60(2), 262–278.
- 462 Witte, M. K., Chuang, P. Y., Ayala, O., Wang, L.-P., & Feingold, G. (2019). Com-
 463 parison of observed and simulated drop size distributions from large-eddy
 464 simulations with bin microphysics. *Monthly Weather Review*, 147(2), 477–493.
- 465 Witte, M. K., Morrison, H., Davis, A. B., & Teixeira, J. (2022). Limitations of bin
 466 and bulk microphysics in reproducing the observed spatial structure of light
 467 precipitation. *Journal of the Atmospheric Sciences*, 79(1), 161–178.
- 468 Wood, R. (2012). Stratocumulus clouds. *Monthly Weather Review*, 140(8), 2373–
 469 2423.
- 470 Wood, R., Comstock, K., Bretherton, C. S., Cornish, C., Tomlinson, J., Collins,
 471 D. R., & Fairall, C. (2008). Open cellular structure in marine stratocumulus
 472 sheets. *Journal of Geophysical Research: Atmospheres*, 113(D12).